















Imaging of twisted monolayers in three-dimensional nanoporous graphene

Oreste De Luca ^{1,2} Antonio Palamara,^{1,3} Michele Pisarra ^{1,3,*} Francesca Mazzei ^{1,3} Tommaso Caruso ^{1,2}
Giovanni Desiderio ⁴ Dario Marchiani ⁵ Riccardo Frisenda ⁵ Samuel Jeong ⁶ Yoshikazu Ito ⁶ Carlo Mariani ⁵
Maria Grazia Betti ⁵ Marco Papagno ^{1,2} Raffaele G. Agostino,^{1,2}

Daniela Pacilé ^{1,†} and Antonello Sindona ^{1,3}

¹*Dipartimento di Fisica, Università della Calabria, Via P. Bucci, I-87036 Rende, Cosenza, Italy*

²*STAR Research Infrastructure, Università della Calabria, Via Tito Flavio, I-87036 Rende, Cosenza, Italy*

³*INFN, sezione LNF, Gruppo collegato di Cosenza, Via P. Bucci, I-87036 Rende, Cosenza, Italy*

⁴*Institute of Nanotechnology, CNR-NANOTEC, Via P. Bucci 31/C, I-87036 Rende, Cosenza, Italy*

⁵*Dipartimento di Fisica, Università di Roma "La Sapienza", I-00185 Roma, Italy*

⁶*Institute of Applied Physics, Graduate School of Pure and Applied Sciences, University of Tsukuba, Tsukuba 305-8573, Japan*



(Received 15 April 2024; revised 13 September 2024; accepted 7 January 2025; published 27 January 2025)

The investigation of intricate alignments in two-dimensional materials has garnered significant attention, fueled by the growing ability to precisely manipulate and engineer electronic properties through controlled stacking and orientation. Recent observations of spontaneous arrangements in multilayer materials with stochastic twist angles offer new opportunities to elucidate the unique physics governing moiré superstructures, and the critical role of the electronic coupling between layers. In this context, the present study focuses on the atomic-scale characterization of nanoporous graphene, with particular emphasis on regions formed by misoriented graphene layers that assemble into crumpled, continuous patterns. Despite the absence of flat domains at the submicron scale, scanning tunneling microscopy is employed to identify dominant twisted multilayer structures in the samples. To complement the experimental observations, a simplified, yet, effective exponential parametric model is introduced, merging independent analytic electron densities to estimate the number of misaligned layers in the scanned areas. This approach is further refined through density-functional theory calculations of projected electron densities from graphene, which are rotated and stacked at adjusted interlayer distances. The synergy between the two models provides a robust framework for distinguishing between twisted bilayer and twisted trilayer domains, as observed in constant-current imaging. Finally, a full density-functional theory analysis is conducted on simple few-layer graphene structures, assessing the role of interlayer correlations. The present study provides an atomic-level description of porous graphene, while also offering accessible tools for simulating twisted layered materials beyond graphene, which may be beneficial for the STM community.

DOI: [10.1103/PhysRevB.111.045432](https://doi.org/10.1103/PhysRevB.111.045432)

I. INTRODUCTION

Practical implementations of two-dimensional (2D) graphene in actual devices are often constrained by the relative small size of graphene flakes, resulting in restricted areal mass loading. This limitation is particularly critical in various applications, including energy storage technologies such as supercapacitors, lithium-ion batteries, fuel cells, and systems for gas separation or storage. Related technological challenges have driven significant advancements in three-dimensional (3D) graphene nanoarchitectures over the past decade [1–3]. These 3D structures are designed to provide porous materials with enhanced surface area and increased capacity for the transport and storage of charged particles, gases, and liquids. However, the transition from 2D to 3D graphene-based materials typically requires trade-offs in the remarkable properties of graphene, such as high electron conductivity,

thermal stability, and mechanical strength [4]. The formation process thus requires careful control over defects and contaminants, which can significantly affect the performance of electronic devices.

Among various growth methods for porous graphene materials, nanoporous graphene (NPG) has emerged as a promising candidate [5–7]. NPG is typically synthesized via Ni-based chemical vapor deposition (CVD), with the resulting NPG samples characterized by centimeter-scale size and exceptionally large surface area, on the order of thousands of m^2/g [8,9]. The material consists of a continuous veil of one to a few slightly interacting layers, with a high degree of crystalline order and negligible defect density [10,11]. Each layer develops into a crumpled structure, featuring pores that extend from several tens of nanometers to a few microns in size. These variations depend on specific growth conditions, primarily parameters governing the CVD process, including exposure time and temperature [8,12]. Recent studies indicate that NPG retains electronic and transport properties akin to those of an ideal 2D graphene sheet [10–13], making it a promising and cost-effective material for integration into practical

*Contact author: michele.pisarra@unical.it

†Contact author: daniela.pacile@fis.unical.it

devices. Moreover, NPG enables the exploration of a wide range of small rotational angles between weakly interacting twisted layers, serving as a versatile experimental platform for investigating exotic electronic and electrical properties, from insulating to superconducting behaviors [14–16]. In this context, precise atomic-scale imaging and analysis are of paramount importance.

Unfortunately, the intricate 3D architectures of graphene-based porous materials often restrict the application of powerful experimental techniques such as scanning tunneling microscopy (STM), which demands flat regions at the sub-micron scale for effective utilization. Nonetheless, this paper presents a challenging experiment conducted on NPG samples, where the atomic structure of NPG is elucidated through the application of STM. The STM images enable the mapping of graphene layers within the material and provide real-space insights into the intricate, misoriented nature of the NPG samples. Fast Fourier transform (FFT) processing of the images offers quantitative information on the number of layers involved in the samples and their relative orientation.

A standard framework for interpreting these measurements is provided by the Tersoff-Hamann scheme [17], grounded in Bardeen's perturbation theory of tunneling [18], in which STM images are modeled as projections of the local density of states within the energy window between the Fermi level and the applied bias. Building on this approach, an exponential parametric model is employed here as an efficient preliminary tool for interpreting both real-space and FFT data, utilizing an analytical expression for the projected electron density in isolated graphene layers [19,20]. To enhance the accuracy of image analysis, a refined method is developed, relying on the electron density of monolayer graphene, computed using density-functional theory (DFT), and projected over the one electron states near the Fermi level selected by an applied bias. This projected density is then replicated at adjusted interlayer distances, with relative rotations between the layers. Although sensitive to fitting parameters, both the analytical and DFT-based approaches demonstrate good to very good agreement with constant-current STM images and their corresponding FFT spots for twisted bilayer and twisted trilayer regions, at precise stacking angles and interlayer distances. For further validation, full DFT calculations are performed on *simple* twisted few-layer configurations, providing deeper insights into the interlayer interactions and electronic properties of multilayer graphene systems.

II. METHODS

Samples of NPG were synthesized via CVD of benzene (C_6H_6) on nanoporous nickel (np-Ni) templates, following established procedures [8,12]. The np-Ni substrate, approximately 30- μm thick, was fabricated by chemically dealloying manganese from a $Ni_{30}Mn_{70}$ precursor in a weak acid solution, resulting in a structure with an average nanopore and ligament size of approximately 10 nm. A layer of graphene was subsequently grown on the np-Ni surface under controlled conditions, with C_6H_6 at 0.5 mbar pressure, and Ar and H_2 flow rates of 200 sccm and 100 sccm, respectively, at 800°C for 120 s. The resultant graphene sheet displayed a 3D morphology mirroring the underlying np-Ni substrate. The

Ni template was finally removed by chemical dissolution in a 1.0 M hydrochloric acid solution, followed by washing and rinsing in distilled water.

Scanning electron microscopy (SEM) images were obtained using a FEI Quanta-FEG 400 microscope with a 15-keV electron beam, revealing the typical morphology of the samples deposited on carbon tape. STM measurements were conducted under ultra-high vacuum (UHV) conditions using an SPM Aarhus 150 system equipped with a KoliibriSensor from SPECS, controlled via the Nanonis Control system. STM images were acquired at room temperature (RT) in constant-current mode, employing a tungsten tip cleaned in UHV by repeated cycles of Ar^+ sputtering. Prior to data acquisition, the NPG samples were degassed in UHV at approximately 600°C for several hours to remove contaminants. During the STM acquisitions, owing to the complexity of the investigated samples, particular attention and time were dedicated to find the right experimental conditions (tip approach, tunneling current, bias voltage, scan's modality, etc.) and enable imaging at the atomic scale. However, these ideal conditions were only achieved in a few instances. Some of these instances are discussed below, with additional examples provided in the Supplemental Material [21]. The acquired STM images were then processed using WSxM software [22].

To simulate the STM images, an analytical model of electron density in graphene was employed as a basic tool [19]. This framework relies on the in-plane (xy) distribution,

$$n_{\parallel}(x, y) = n_0 \phi_{\parallel}(x, y), \quad (1)$$

where n_0 denotes the number of occupied band states per unit volume around the Dirac cone, and

$$\begin{aligned} \phi_{\parallel}(x, y) = & 1 - \frac{1}{3} \cos \left[\frac{2\pi}{a} \left(x + \frac{y}{\sqrt{3}} \right) \right] \\ & - \frac{1}{3} \cos \left[\frac{2\pi}{a} \left(x - \frac{y}{\sqrt{3}} \right) \right] - \frac{1}{3} \cos \left(\frac{4\pi y}{\sqrt{3}a} \right) \end{aligned} \quad (2)$$

is a smooth periodic function of the monolayer, defined by the lattice constant $a \approx 2.46 \text{ \AA}$, with the origin of the coordinate system set at the center of one of the hexagones of the graphene honeycomb arrangement. The normalization in Eq. (2) ensures that $\phi_{\parallel}(x, y)/S_c$ can be interpreted as the position probability distribution for a valence Dirac cone electron on the unit-cell surface $S_c = a^2\sqrt{3}/2$.

The total electron density of twisted m -layer graphene was then modeled as the sum of electron densities $n_{\parallel}(x_i, y_i)$ for $i = 1, \dots, m$, with rotated in-plane coordinates $x_i = x \cos \theta_i - y \sin \theta_i$ and $y_i = x \sin \theta_i + y \cos \theta_i$, determined by the twist angle θ_i of the i th plane. The in-plane densities were offset by a typical distance of $d = 3.34 \text{ \AA}$, corresponding to the separation between adjacent graphene planes in graphite. Specifically, they were positioned at out-of-plane coordinates $z_i = -(i-1)d$ and combined using exponential parametric functions along the rotation axis (z) as follows:

$$n(x, y, z) = \frac{n_0}{m} \sum_{i=1}^m \phi_{\parallel}(x_i, y_i) e^{-\frac{|z-z_i|}{\lambda}}. \quad (3)$$

The topmost graphene layer ($i = 1$) was taken as the reference, placed at $z_1 = 0$, and left unrotated, with $\theta_1 = 0$. Notably, the normalization imposed on Eq. (2) also ensures that $n(x, y, z)/n_0\Omega_0$ represents the position probability distribution for an electron, from an occupied Dirac cone state, within the characteristic volume $\Omega_0 = 2\lambda S_c$. Accordingly, $n_0\Omega_0$ denotes the number of valence electrons in the unit cell, determined by the bias voltage. Equation (3) provides the electron density of decoupled, misaligned layers, projected onto their valence electrons near the Fermi level, as established in previous study [20]. The interlayer attenuation length λ is the free parameter of the approach, adjustable through additional self-consistent calculations or experiments.

A more robust and versatile tool for image analysis was here developed based on DFT calculations of the projected electron density $n_b(x, y, z)$ in monolayer graphene (MG) (see also Appendix A). n_b is here obtained selecting the one-electron states in the energy window going from the Fermi level (set to 0 throughout this paper) to the bias energy, $E_b = eV_b$, where V_b a specific bias voltage and e is the electron charge. In this DFT-uncorrelated (DFT-U) scenario, the projected electron density of the multilayer structure is obtained by superimposing the contributions from each twisted layer through

$$n(x, y, z) = \sum_{i=1}^m n_b(x_i, y_i, z - z_i), \quad (4)$$

where the layers are stacked at a distance d , serving as the free parameter of the method.

In this case as well, the electron density is obtained as a sum of the densities of each graphene plane, neglecting interlayer interactions. While this approach represents a significant simplification, previous theoretical [23] and experimental studies [24,25] have shown that in TBG systems, for twist angles away from the *magic condition* (i.e., greater than $\sim 3^\circ$), the conical band dispersion characteristic of each single layer remains intact. This observation suggests that treating the layers in multilayer twisted graphene as effectively decoupled is reasonable for *large* twist angles. This fact is further discussed in Sec. III.

The reliability of the analytical and DFT-U imaging tools, defined by Eqs. (3) and (4), respectively, was validated against full DFT simulations on twisted bilayer graphene (TBG) and selected configurations of twisted trilayer graphene (TTG). This validation enabled more accurate insights into interlayer coupling.

All DFT calculations were run using the plane-wave basis, as implemented in the QUANTUM ESPRESSO (QE) package [26,27]. The generalized gradient approximation (GGA) was employed within the Perdew-Burke-Ernzerhof (PBE) parametrization of the exchange-correlation functional [28]. An optimized norm-conserving pseudopotential of the Vanderbilt type was adopted to eliminate the core electrons of the carbon atoms [29], in conjunction with an energy cutoff of 45 Ha on the plane waves and a convergence criterion of 10^{-6} eV on the self-consistent cycle. A vacuum region of 30 Å was maintained between the replicated slabs, while differently resolved meshes of $48 \times 48 \times 1$, $18 \times 18 \times 1$, and $12 \times 12 \times 1$ were used in the Brillouin zone sampling for MG, TBG,

and TTG, respectively. The optimized ground-state electron densities, generated by the occupied band states lying a few hundred meV below the Fermi level, were used to obtain spatially resolved projected densities. In particular, we selected $E_b = -0.45$ eV and $E_b = -0.80$ eV as the lower integration limits in projected density calculations on TBG and TTG, respectively, to match the bias voltage values $V_b = -0.45$ V and $V_b = -0.80$ V used in the experimental acquisition of the STM images (see Sec. III). It is worth noting that at $\sim \pm 0.8$ eV the band dispersion of freestanding graphene begins to exhibit anisotropic, nonconical features. Consequently, $E_b \sim \pm 0.8$ eV represent the upper and lower limits of applicability of the methods outlined in this work. The DFT projected densities were then compared to $n(x, y, z)$, as given by Eqs. (3) and (4), for $m = 1, 2, 3$. It was observed that the analytical model reasonably accounts for the behavior of occupied electron states around the Fermi level of the few-layer structures, at attenuation lengths λ of the order of ~ 0.5 Å and distances z of the order of ~ 2 Å from the reference lattice plane. Additional important details on the applicability of Eq. (3) are discussed in Appendices A–C. It was further established that the DFT-U model gives results fully consistent with DFT predictions at the interlayer distance $d = 3.34$ Å.

Within the framework of the Tersoff-Hamann theory [17], we assumed that the STM current has the same spatial dependence of the electron density, so that it is modeled as

$$I_{\text{STM}} = \frac{I_0}{n_0} n(x, y, z), \quad (5)$$

where I_0 represents the density-to-current conversion factor, and $n(x, y, z)$ is the density output from the above outlined analytical and DFT-U approaches with optimized λ and d parameters, respectively, which effectively regulates the transport of electrons to the STM tip. Constant-current STM images were then computed by fixing I_{STM} to a constant value and solving Eq. (5) for $z > 0$. In the analytical framework of Eq. (3), this step leads to

$$z(x, y) = z_0 + \lambda \ln \left[\frac{1}{m} \sum_{i=1}^m \phi_{\parallel}(x_i, y_i) e^{\frac{z_i}{\lambda}} \right] \quad (6)$$

with $z_0 = \lambda \ln(I_0/I_{\text{STM}})$. In DFT-U calculations, n_0 was estimated as the number of electrons, selected by the bias voltage, per unit cell or slab volume. Then, Eq. (5) was solved numerically for $z > 0$.

2D-FFT analysis was performed by examining the intensity maps of the modulus of the Fourier transformed constant-current surfaces onto the wave vector (k_x, k_y) domain, namely,

$$\tilde{z}(k_x, k_y) = |\text{FFT}[z(x, y)]_{x \rightarrow k_x, y \rightarrow k_y}|. \quad (7)$$

III. RESULTS AND DISCUSSION

The NPG samples were demonstrated to possess a well-defined 3D porous structure, characterized by continuous membranes with smooth edges, free from irregular fraying [10,11]. The SEM images in Fig. 1 detail the morphological characteristics of these samples across various length scales. Specifically, Fig. 1(a) reveals deep cavities extending over hundreds of micrometers. The inset in Fig. 1(a) presents a

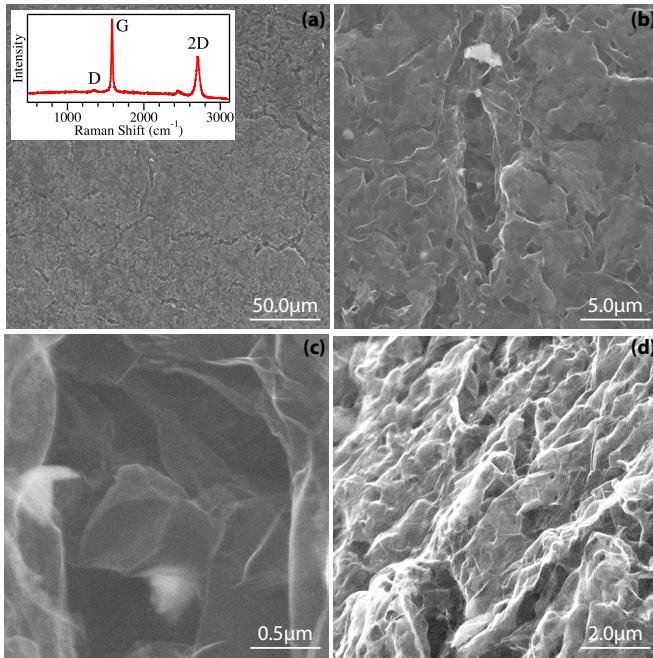


FIG. 1. SEM images of NPG acquired at scales of (a) 50.0 μm , (b) 5.0 μm , (c) 0.5 μm , and (d) 2.0 μm (with lateral resolution). The inset in (a) shows a micro-Raman spectrum of NPG under UHV. Panel (c) provides a higher resolution image of the central cavity from (b).

representative micro-Raman spectrum, showing prominent G (1580 cm^{-1}) and 2D (2700 cm^{-1}) band peaks [30]. The 2D band lineshape, associated with the breathing modes of carbon-atom rings, appears featureless and more symmetric compared to that of bi- and trilayer graphene, in which a clear convolution of distinct subpeaks is observed [31–33]. In contrast, the varying angles within the weakly interacting layers of NPG give rise to a broad 2D peak, similar to that seen in turbostratic multilayer graphene [31]. Additionally, the relatively small D band peak at 1350 cm^{-1} indicates an NPG structure with minimal defects [30].

At higher resolutions, Fig. 1(b) reveals cavities and pores several micrometers wide, which are further detailed in the magnified image at the micrometer scale shown in Fig. 1(c). The lateral perspective in Fig. 1(d) reflects the absence of planar regions over tens of micrometers, thereby underscoring the intrinsic challenges of applying STM techniques to NPG materials. In summary, the SEM analysis in Fig. 1 attests that the NPG samples exhibit a crumpled sheet structure.

Further scrutiny is required to elucidate the role of interlayer interactions, including the relative distances and orientations between graphene planes. Prior investigations employing high-resolution (HR) transmission electron microscopy (TEM) have shown diverse orientations among the graphene sublayers in NPG, evidenced by prominent hexagonal moiré superstructures [10]. These findings also strongly suggest the prevalence of misoriented bilayers within the samples, consistent with observations from Raman spectroscopy [8]. Nevertheless, a direct investigation into the atomic-scale structural configuration of NPG remains lacking.

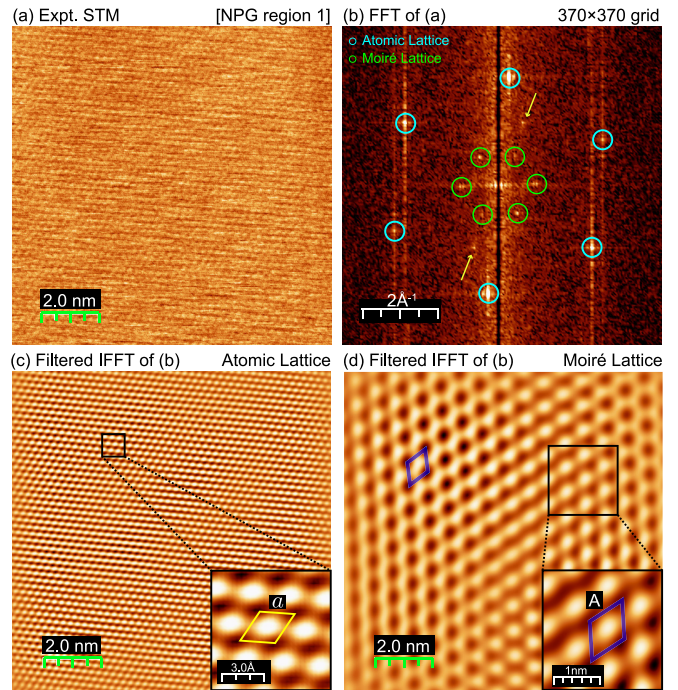


FIG. 2. (a) STM image of an NPG domain (NPG region 1) acquired with a tunneling current of 0.25 nA and a bias voltage of -0.45 V . (b) FFT of (a) on a 370×370 grid, showing two prominent, approximately hexagonal sets of outer (atomic) and inner (moiré) spots, marked by cyan and green circles, respectively. The average distances of these sets from the center yield lattice constants of $a = 2.46 \pm 0.04\text{ \AA}$ and $A = 7.8 \pm 0.3\text{ \AA}$. A pair of spots between the nearly hexagonal contours is also visible, indicated by yellow arrows. (c) IFFT of the cyan spots filtered from (b), revealing the real-space atomic pattern with the unit cell outlined in yellow. (d) IFFT of the green spots filtered from (b), revealing the real-space moiré pattern with the unit cell outlined in blue.

The STM analyses carried out in this paper demonstrate that the NPG samples exhibit small graphene terraces, tens of nanometers wide, with manifolds of either single or multiple moiré periodicities.

To begin with, Fig. 2(a) presents an HR-STM topographic image of a domain, designated as NPG region 1. The scan reveals a graphene texture characterized by a triangular structure, which is consistent with sublattice asymmetry in graphite [34] and indicative of interlayer coupling. The FFT image of Fig. 2(a), shown in Fig. 2(b), reveals two distinct periodicity scales characterized by an atomic pattern (cyan circled spots, outer hexagon) and a moiré pattern (green-circled spots, inner hexagon). The estimated lattice parameters are $a = 2.46 \pm 0.04\text{ \AA}$, consistent with the graphene lattice constant, and $A = 7.8 \pm 0.3\text{ \AA}$, which corresponds to the moiré superlattice periodicity resulting from the relative twist between the graphene layers. Specifically, the two hexagonal patterns identify a TBG structure with $\theta_1 = 0$ and $\theta_2 = 18^\circ \pm 2^\circ$, as determined from the relation $\theta = 2 \arcsin(a/2A)$ [35]. To better illustrate this point, two filtered images were obtained by separately selecting the outer and inner hexagons from Fig. 2(b) and processing the filtered FFT data with the inverse FFT (IFFT) algorithm. The topographies of these patterns are

shown in Figs. 2(c) and 2(d), which separately depict the atomic and moiré features in real space, with unit cells marked by yellow and blue lines, respectively. The combined IFFT, obtained by selecting both hexagons of different periodicity from Fig. 2(b), is displayed in Fig. 3(a). Here, the interplay between moiré and atomic domains is highlighted by the different orientations of the two unit cells. Additional insights are provided in Fig. 3(b), which shows the IFFT of Fig. 2(b), processed with an intensity cutoff above 6% of the maximum. This image elucidates the appearance of the moiré lattice at the atomic lattice scale.

Preliminary theoretical support for the experimental findings in Fig. 2 is provided by the exponential parametric model described in Sec. II. In particular, several constant-current profiles were determined using Eqs. (3) and (6) for a bilayer graphene lattice with standard atomic geometry and a twist angle of 18° . The simulations examined various constant-current levels, with I_{STM}/I_0 ranging from 0.1 to 0.9, to fix the overall intensity scale of the resulting image, and explored attenuation lengths λ from 0.5 \AA to 5.0 \AA , to regulate the contribution of the bottom sublayer to the image. As a notable example, Fig. 3(c) presents a constant-current STM image computed with $I_{\text{STM}}/I_0 = 0.25$ and $\lambda = 5.0 \text{ \AA}$. The visual output exhibits patterns similar to those observed experimentally in Fig. 3(a), with nearly identical arrangements of atomic and moiré unit cells. The inset in Fig. 3(c) shows a magnified view at the atomic lattice scale, where the atomic pattern (green spots) aligns closely with that in Fig. 3(b). A different perspective on this feature is given in Fig. 3(d), which displays the STM constant-current image generated with the reduced attenuation length $\lambda = 0.5 \text{ \AA}$. By construction, this image preserves the atomic lattice periodicity observed in the inset of Fig. 3(c), consistent with the experimentally derived pattern shown in Fig. 3(b). However, no moiré patterns are detectable.

The FFT analysis of the simulated real-space images reveals additional quantitative information. In particular, Fig. 3(e) presents the FFT of Fig. 3(c), calculated via Eq. (7) on a 1024×1024 grid. In this analysis, the constant-current level I_{STM}/I_0 was increased to 0.65 to better isolate the main patterns owing to the atomic and moiré lattices, being again marked by cyan and green circles. The relative distances between the two hexagonal patterns from the image center enable the extraction of the atomic lattice constant $a = 2.46 \text{ \AA}$ and the moiré lattice constant $A = 7.76 \text{ \AA}$. The former is an input parameter of the simulation. The latter arises from the twist angle, closely matching the experimental value derived from Fig. 2(b). Furthermore, the position of the main spots in Fig. 3(e) is in excellent agreement with the noise-reduced FFT image of Fig. 3(f), whose real-space features are displayed in the IFFT image of Fig. 3(b). Nevertheless, the experimental and simulated FFT images exhibit differences in relative intensities. In particular, the experimental FFT shows a predominant contribution from the atomic lattice of the top graphene sublayer, indicated by the cyan circles in Fig. 3(f). The simulated FFT, in contrast, shows marked contributions from both the top and bottom graphene layers, denoted by solid and dashed cyan circles in Fig. 3(e). Notably, the moiré lattice spots, marked by green circles, exhibit similar relative intensities in both the experimental and simulated FFTs

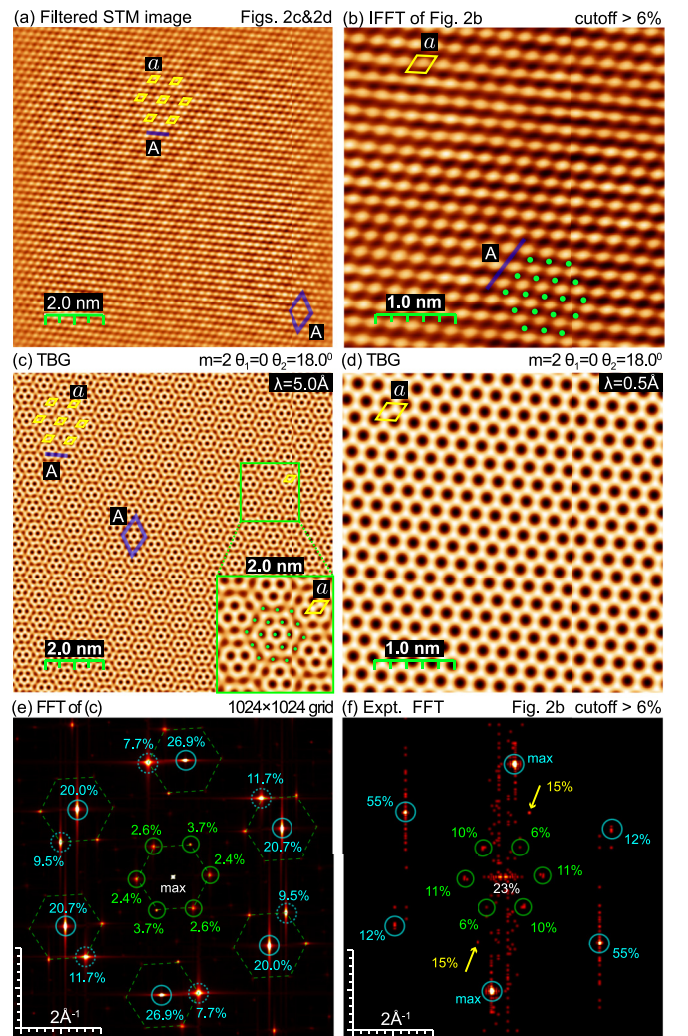


FIG. 3. (a) IFFT image isolating both atomic and moiré FFT spots from Fig. 2(b). (b) IFFT image of the FFT data in (f), filtered from Fig. 2(b) on a 370×370 grid with an intensity cutoff above 6% of the maximum. (c) Constant-current STM image of TBG obtained using Eqs. (2) and (6) with $m = 2$, $\theta_2 = 18^\circ$, $a = 2.46 \text{ \AA}$, $d = 3.34 \text{ \AA}$, $I_{\text{STM}}/I_0 = 0.25$, and $\lambda = 5.0 \text{ \AA}$. (Inset) Magnified atomic-scale feature. (d) Constant-current STM image as in (c) but with $\lambda = 0.5 \text{ \AA}$. In (a)–(d), yellow hexagons and blue parallelograms mark the atomic and moiré unit cells, respectively. Green spots replicate the atomic pattern. (e) FFT of a constant-current STM image computed using Eqs. (2), (6), and (7) with $I_{\text{STM}}/I_0 = 0.65$, while all other parameters remain as in (c). Atomic spots corresponding to the top and bottom layers are marked by solid and dashed cyan circles, representing the lattice constant $a = 2.46 \text{ \AA}$. Moiré spots are indicated by green circles, corresponding to $A = 7.76 \text{ \AA}$, with associated hexagonal contours marked by dashed lines. (f) Noise-reduced FFT image of Fig. 2(b), highlighting atomic (cyan) and moiré (green) spots, with additional distorted features marked by yellow arrows, which are reflected in the IFFT image in (b). Spot intensities in (e) and (f) are given as a percentage of the maximum.

around the image center. Additionally, the experimental FFT images, in both their original and noise-reduced forms, reveal a couple of high-intensity spots between the hexagonal patterns, indicated by yellow arrows in Figs. 2(b) and 3(f). These

features may suggest distorted effects, potentially caused by some waving between the graphene layers.

Thus, the real-space and reciprocal-space images in Fig. 3 support the conclusion that the NPG region 1, shown in Fig. 2, corresponds to a TBG lattice with a twist angle of approximately 18° . Interestingly, the double pattern in Fig. 3(e) remains detectable even when the real-space image is simulated with an attenuation length of 0.75 to 1.0 Å, as reported within the Supplemental Material [21] (see Fig. S1). However, in these instances, the relative intensities of the moiré spots are significantly lower. Furthermore, when λ approaches 0.5 Å, the moiré structure tends to be hardly identifiable. This indicates that the analytical model with realistic parameters does not fully capture the contribution of the sublayer to the STM current. Specifically, an attenuation length λ approximately ten times larger than expected is required to reproduce the experimental moiré pattern, which consequently leads to an overestimation of the density decay from the bottom graphene layer, as noted in previous studies [20]. Nonetheless, setting λ to 5.0 Å appears to compensate for the underestimation of the tunneling current from the bottom layer to the tip, as described by the proportionality relation (5).

To clarify this issue, comparative calculations were performed using DFT, focusing on a TBG system arranged in the commensurate lattice [23,36–38] that closely matches the experimental observations in Fig. 2. The commensurate TBG structure was generated with a twist angle of 17.8966° , where the rotation axis passes through aligned atomic sites in the top and bottom layers. This configuration results in a total of 124 carbon atoms, equally distributed between two graphene supercells with a combined area of $1.62466 \times 10^2 \text{ \AA}^2$ (refer to Appendix B for further details). The projected density from the system, with an applied bias voltage V_b of -0.45 V , accounted for 0.77778 electrons in the slab volume $3.24932 \times 10^3 \text{ \AA}^3$, yielding $n_0 = 2.39366 \times 10^{-4} \text{ \AA}^{-3}$. The DFT constant-current profiles were determined by plugging the computed projected density into Eq. (5) and numerically solving it for $z > 0$. During this process, different I_{STM}/I_0 levels were examined between 0.05 and 0.20. The corresponding FFT images were then obtained using Eq. (7). The STM constant-current image calculated by DFT with $I_{\text{STM}}/I_0 = 0.075$ is shown in Fig. 4(a), which appears indistinguishable from Fig. 3(d) despite using a different constant-current level. This similarity indicates that Eq. (6) provides a reliable projected density for TBG at $\lambda = 0.5 \text{ \AA}$, apart from an overall intensity scale factor, i.e., the value of I_{STM}/I_0 . The FFT of Fig. 4(a), shown in Fig. 4(b) with an enhanced constant-current level I_{STM}/I_0 of 0.200, also demonstrates the prominent contribution of the atomic lattice of the unrotated TBG layer, while revealing a series of faint spots. Among these spots, a hexagonal structure can be identified, set by the lattice constant $A = 7.91 \text{ \AA}$, which resembles the experimental and simulated moiré patterns of the incommensurate TBG lattice shown in Figs. 3(e) and 3(f). Notably, the spots associated with the atomic lattice of the rotated TBG layer exhibit very low to undetectable intensities, consistent with the experimental FFT image in Fig. 2(b). Other secondary spots are observed that account for the commensurate periodicity. However, the numerical procedure used to solve Eq. (5) introduces numerical uncertainties in the FFT algorithm, resulting in slight

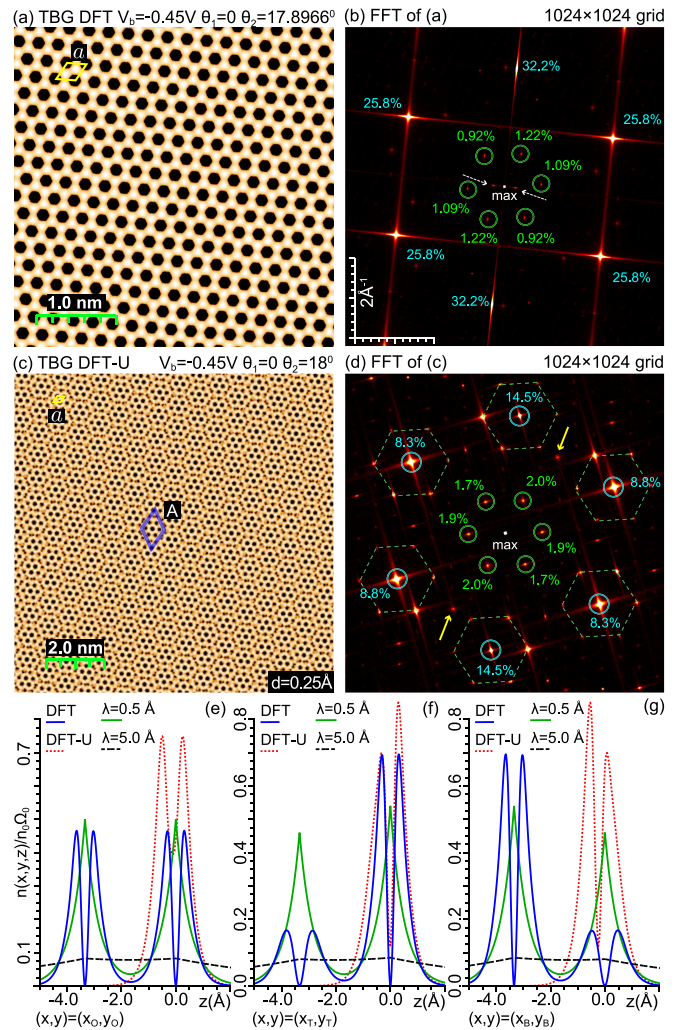


FIG. 4. (a) Constant-current STM image of a commensurate TBG ($\theta_1 = 0$, $\theta_2 = 17.8966^\circ$, $a = 2.46 \text{ \AA}$, $d = 3.34 \text{ \AA}$), obtained using DFT and Eq. (5), with parameters $V_b = -0.45 \text{ V}$, and $I_{\text{STM}}/I_0 = 0.075$. (b) FFT of the STM image in (a), computed using Eq. (7) on a 1024×1024 grid with $I_{\text{STM}}/I_0 = 0.200$, while retaining all other parameters from (a). The color scheme matches the legend in Fig. 3(f), with faint spots, marked by dashed arrows, indicating commensurate periodicity. (c) Constant-current STM image of TBG generated from DFT-U calculations using Eqs. (4) and (5), with parameters: $\theta_1 = 0$, $\theta_2 = 18^\circ$, $a = 2.46 \text{ \AA}$, $d = 0.25 \text{ \AA}$, $V_b = -0.45 \text{ V}$, and $I_{\text{STM}}/I_0 = 0.050$. (d) FFT of the STM image in (c), calculated using Eqs. (4), (5), and (7) on a 1024×1024 grid with $I_{\text{STM}}/I_0 = 0.150$, employing the same color scheme as in Fig. 3(e). (e)–(g) Projected density of TBG along the out-of-plane axis (z), computed using: DFT with parameters as in (a); DFT-U with parameters as in (c); and Eq. (3) with parameters from Figs. 3(c) ($\lambda = 5.0 \text{ \AA}$) and 3(d) ($\lambda = 0.5 \text{ \AA}$). Vertical sections are taken at in-plane coordinates with maximum density: (e) (x_0, y_0) , where the top and bottom sublattice sites align; (f) (x_T, y_T) at a top sublattice site; and (g) (x_B, y_B) at a bottom sublattice site. All curves are normalized to unit area.

displacements in their expected positions. Thus, even when using Eq. (5) in combination with DFT calculations, the effect of the bottom TBG layer is underestimated. To expand the exploration beyond the analytical approach while preserving the simplicity of Eq. (5), the DFT-U method outlined in Sec. II

was employed. Accordingly, the projected density of graphene under a bias voltage of $V_b = -0.45$ V was computed using DFT (see Appendix A for further details). This projected density was then replicated across a range of interlayer separations, varying from 0.20 Å to 3.34 Å. Subsequently, a rotation by 18° was applied to the projected density of the bottom layer. Figure 4(c) displays the constant-current STM image calculated using the DFT-U approach, as detailed in Eqs. (4) and (5), with $I_{\text{STM}}/I_0 = 0.050$ and an interlayer separation of $d = 0.25$ Å. This image closely resembles the textures seen in the filtered experimental image of Fig. 3(a) and aligns well with the analytical model results in Fig. 3(c), obtained using an attenuation length of $\lambda = 5.0$ Å. The FFT of Fig. 4(c), shown in Fig. 4(d) with an enhanced constant-current level of $I_{\text{STM}}/I_0 = 0.150$, closely aligns with the FFT derived from the analytical model in Fig. 3(e), yielding a moiré lattice constant $A = 7.80$ Å. Additionally, Fig. 4(d) reveals two extra spots that resemble the distorted features observed in the filtered experimental image in Fig. 3(f), appearing at similar positions. These findings demonstrate that increasing the attenuation significantly beyond the expected value of 0.5 Å effectively mimics the effect of reducing the interlayer separation to values smaller than the equilibrium distance of 3.34 Å. This reduction, in turn, compensates for the underestimation of the tunneling current from the bottom graphene layer to the STM tip, as predicted by Eq. (5).

A deeper understanding of the relationship between the projected electron densities n , and the STM current, beyond Eq. (5), is achieved by comparing the out-of-plane behavior of the n derived from the analytical, DFT-U, and DFT approaches. This analysis involved identifying in-plane coordinates where n function reaches its maximum values. One such coordinate, (x_o, y_o) , lies along the rotation axis of the commensurate TBG lattice, where atomic sites in the top and bottom layers align. The corresponding out-of-plane density profile, $n(x_o, y_o, z)$, reflects an equal distribution of outer valence electrons around the TBG layers, as shown in Fig. 4(e). Another coordinate, (x_T, y_T) , represents the nearest-neighbor atomic site in the top layer relative to the rotation axis in the incommensurate TBG lattice, located at the center of the hexagonal unit cell of the layer. The out-of-plane density profile at this coordinate, $n(x_T, y_T, z)$, shows maximal electron localization around the top layer, as depicted in Fig. 4(f). A third coordinate, (x_B, y_B) , corresponds to the nearest-neighbor atomic site in the bottom layer to the rotation axis in the incommensurate TBG lattice. The associated density profile, $n(x_B, y_B, z)$, shows maximal electron localization around the bottom layer, as illustrated in Fig. 4(g). The selected coordinates, (x_o, y_o) , (x_T, y_T) , and (x_B, y_B) , along with the rotation axes, are highlighted in Fig. 10 in Appendix B, providing a spatial reference for the observed trends in the density profiles.

In Figs. 4(e)–4(g), the full DFT calculations on commensurate TBG (blue lines) provide the most accurate description of n , underscoring the importance of interlayer correlations in the system. The analytical model with $\lambda = 0.5$ Å offers the closest approximation to this behavior (green lines). However, owing to its construction, as defined by Eqs. (2) and (3), this model cannot capture the p_z character of the outer valence electrons around the TBG layers and tends to overestimate

electron localization between the planes. Although not shown in Figs. 4(e)–4(g), the DFT-U results with $d = 3.34$ Å closely match the full DFT results. Conversely, the STM current is best represented by the analytical model with $\lambda = 5.0$ Å (dashed-black lines) and the DFT-U result with $d = 0.25$ Å (dashed-red lines), as shown in Figs. 3(c), 3(e), 4(c), and 4(d). In the former case, the increased attenuation length results in a nearly flat profile, while in the latter, the reduced interlayer distance produces a sharply peaked distribution localized around the top layer. In both models, the bottom layer significantly influences STM imaging simulations, a role that is marginal in the DFT results of the commensurate structure. The extreme values of the parameters compensate for the lack of a detailed description of the current flowing from both layers to the STM tip, between the two layers and from both layers to the ground. A more realistic approach would involve incorporating electron transport at the DFT level, which entails a formidable computational effort for the systems analyzed in this work owing to the very large lateral size of the moiré unit cell. On the other hand, both the analytical and DFT-U methods offer practical parametric approaches that yield high-quality results. Additionally, these methods are particularly advantageous for exploring twisted multilayer structures, a task that is computationally prohibitive for DFT, even when merely calculating some ground state properties as the projected electron density.

It is therefore instructive to report measurements that reveal NPG domains exhibiting complexities surpassing those of TBG. Indeed, by examining various areas of the NPG samples, several multilayered structures with different twist angles were observed, as detailed below and in the Supplemental Material [21] (see Fig. S2 and the corresponding Table). Additionally, single-layer graphene structures without extra-periodicity were never detected. This absence is likely caused by the sparse presence of “pure” graphene areas in NPG, as well as the intrinsic instability of a single sheet under the STM tip for this type of material.

Progressing to the multilayer analysis, Figs. 5(a) and 6(a) present constant-current STM measurements of patterns resulting from imaging graphene layers with different misorientations in two specific sampled areas, referred to as NPG region 2 and NPG region 3. The corresponding FFT images in Figs. 5(c) and 6(c) clarify the existence of several superlattices that generate concentric hexagonal spots of decreasing size, highlighted within a dashed-yellow circle. For NPG region 2, using the distance from the image center of each series of spots, the following periodicities are obtained: $A_o = 9.8 \pm 0.3$ Å, $A_i = 44.5 \pm 1.5$ Å, and $A_r = 21.5 \pm 1.0$ Å. Notably, the periodicities of the innermost (A_i) and outermost (A_o) moiré structures are clearly visible in the real-space image of Fig. 5(a), whereas an intermediate hexagonal pattern in the FFT, associated with A_r , is not observed. Similarly, the FFT analysis of NPG region 3, shown in Fig. 6(c), yields $A_o = 14.5 \pm 0.5$ Å, $A_r = 38.5 \pm 1.5$ Å, and $A_i = 40 \pm 2$ Å. Again, A_i and A_o are easily identified in the real-space image of Fig. 6(a), while the intermediate structure associated with A_r , if present, would be difficult to distinguish from that associated with A_i .

To explore the real and reciprocal space features of NPG regions 2 and 3, simulations of a TTG lattice were conducted.

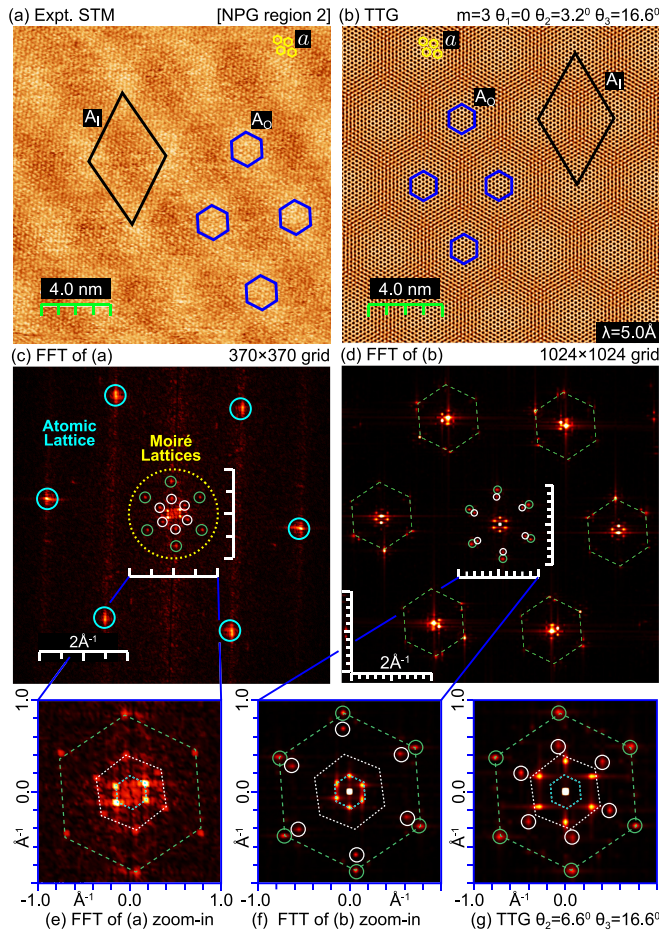


FIG. 5. (a) Constant-current STM image of NPG (region 2) acquired with a tunneling current of 0.75 nA and a bias voltage of -0.80 V. (b) Simulated constant-current STM image of a TTG lattice using Eqs. (3) and (6), with parameters $m = 3$, $\theta_2 = 3.2^\circ$, $\theta_3 = 16.6^\circ$, $a = 2.46$ Å, $d = 3.34$ Å, $I_{\text{STM}}/I_0 = 0.35$, and $\lambda = 5.0$ Å. In both (a) and (b), yellow hexagons indicate the atomic lattice, while black lines and cyan hexagons outline two moiré lattices. (c) FFT of (a) on a 370×370 grid, revealing four sets of hexagonal spots associated to periodicities: $a = 2.46 \pm 0.04$ Å outside the dashed-yellow circle, and $A_o = 9.8 \pm 0.3$ Å, $A_R = 21.5 \pm 1.0$ Å, $A_I = 44.5 \pm 1.5$ Å inside. (d) FFT of (b) on a 1024×1024 grid with $I_{\text{STM}}/I_0 = 0.65$, showing similar spot patterns as (c), with moiré periodicities $A_I = 44.0$ Å and $A_o = 8.60$ Å, along with their replicas at $A_R = 10.50$ Å, and the atomic pattern at $a = 2.46$ Å. (e) Zoom-in of (c) around the central region, focusing on moiré lattices and their replicas. (f) Zoom-in of (d) around the central region, matching the area of (e). (g) FFT a constant-current STM image with the same parameters as in (b), but with a different twist angle of $\theta_2 = 6.6^\circ$, showing the same region as (e) and periodicities $A_I = 22.80$ Å, $A_o = 8.60$ Å, and $A_R = 14.00$ Å. Hexagonal dashed lines in (e)–(g) with the same color delimit equivalent regions in reciprocal space for easier comparison.

Accordingly, the analytical approach outlined in Eqs. (3) and (6) was applied with $m = 3$ at a fixed attenuation length of $\lambda = 5.0$ Å. Various misalignment configurations, defined by θ_2 and θ_3 , were tested through a fitting procedure against the FFT spots in Figs. 5(c) and 6(c).

In particular, the twist angle θ_3 was varied between 9.0° and 18.0° to reproduce the outermost moiré FFT spots, while

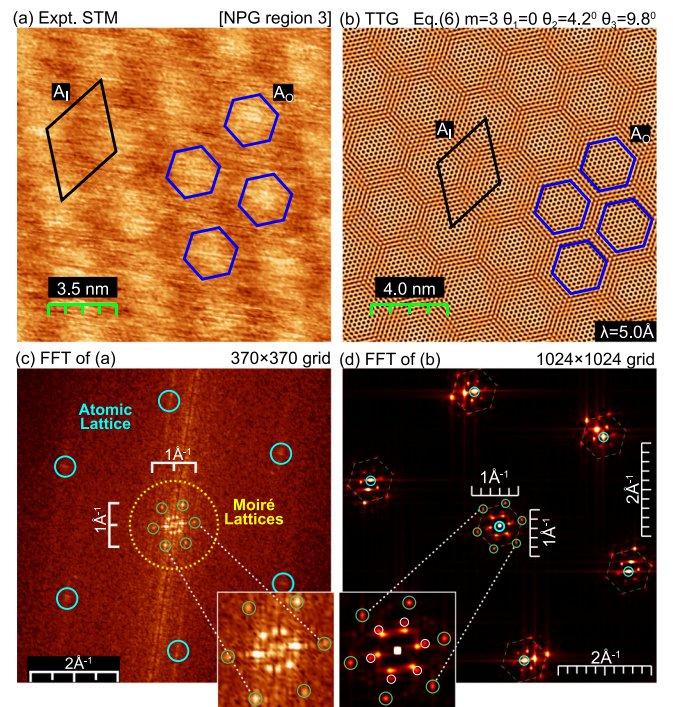


FIG. 6. (a) Constant-current STM image of an NPG (region 3), acquired with a tunneling current of 1.05 nA and a bias voltage of -0.80 V. (b) Simulated constant-current STM image of a TTG lattice using Eqs. (3) and (6) with parameters $m = 3$, $\theta_2 = 4.2^\circ$, $\theta_3 = 9.8^\circ$, $a = 2.46$ Å, $d = 3.34$ Å, $I_{\text{STM}}/I_0 = 0.35$, and $\lambda = 5.0$ Å. In both (a) and (b), black lines and cyan hexagons delineate two patterns attributed to distinct moiré lattices. (c) FFT of (a) on a 370×370 grid, revealing four sets of hexagonal spots corresponding to periodicities: $a = 2.46 \pm 0.04$ Å outside the dashed yellow circle, and $A_o = 15.0 \pm 0.5$ Å, $A_R = 38.5 \pm 1.5$ Å, $A_I = 40 \pm 2$ Å inside. (d) FFT of (b) on a 1024×1024 grid with $I_{\text{STM}}/I_0 = 0.65$, showing similar spot patterns as (c), with periodicities: $a = 2.46$ Å, $A_o = 14.5$ Å, $A_R = 25.0$ Å, and $A_I = 34.0$ Å. Insets in (c) and (d) provide a zoomed view of the central moiré spots.

θ_2 was adjusted within the range of 3.0° to 5.0° to capture the innermost moiré FFT spots. The combination of these two twist angles consistently generated an intermediate pattern in all simulations, corresponding to the hexagonal structure highlighted by green circles in Figs. 5(d) and 6(d). This pattern was interpreted as a replica of the two moiré lattice spots. The appearance of such replicas in the FFT images is typically attributed to the projection method used in generating the constant-current STM image. Interestingly, additional replicated spots were observed at lower constant-current levels, achieved by reducing the value of I_{STM}/I_0 in Eq. (6). Despite the wide range of possible values for the relative twist angles θ_2 and θ_3 , achieving a perfect match between the experimental and simulated images proved challenging.

For NPG region 2, the atomic and moiré patterns shown in Figs. 5(a) and 5(c) were found to align well with the analytical simulations conducted using the twist angles $\theta_2 = 3.2^\circ$ and $\theta_3 = 16.6^\circ$, as illustrated in Figs. 5(b) and 5(d). The TTG lattice of this particular configuration is depicted in Fig 13(a) of Appendix C. In particular, a unit cell with lattice constant

A_1 in Fig. 5(a) is distinctly visible in the simulated constant-current image of Fig. 5(b). The FFT spots shown in Fig. 5(d), derived from Fig. 5(b), form a double moiré superlattice with an intermediate set of replicas centered around an atomic structure, closely resembling the experimental FFT image in Fig. 5(c). The atomic contribution is fixed by the choice of the input parameter $a = 2.46 \text{ \AA}$. In Fig. 5(d), the outermost and innermost hexagonal spots correspond to lattice constants $A_0 = 8.6 \text{ \AA}$ and $A_1 = 44.0 \text{ \AA}$, which are in good agreement with the experimental values observed in Fig. 5(c). The hexagonal replicas suggest a lattice constant A_R of 10.50 \AA , which appears similar to the moiré lattice A_0 in Figs. 5(a) and 5(b), and differs significantly from the result in Fig. 5(c). For closer examination, the experimental and simulated moiré lattices are zoomed in Figs. 5(e) and 5(f), respectively. Additionally, Fig. 5(g) shows another case obtained under the same conditions as Fig. 5(f), but with $\theta_2 = 6.6^\circ$ and $\theta_3 = 16.6^\circ$. The outermost hexagonal spots in Fig. 5(e) are accurately reproduced by the twist angle $\theta_3 = 16.6^\circ$, as indicated by the green-circled spots in Figs. 5(f) and 5(g). Conversely, the innermost moiré spots are better reproduced with the twist angle $\theta_2 = 3.2^\circ$, as shown in Fig. 5(f). Nevertheless, the combination of $\theta_2 = 3.2^\circ$ and $\theta_3 = 16.6^\circ$ results in an incorrect positioning of the intermediate replicas, which are more accurately described by the combination of $\theta_2 = 6.6^\circ$ and $\theta_3 = 16.6^\circ$, as seen in Fig. 5(g).

For NPG region 3, a preliminary analysis was carried out on the experimental STM image in Fig. 6(a) and its corresponding FFT in Fig. 6(c), starting with a TBG lattice with a twist angle of 9.8° . The simulated FFT profile was found to perfectly reproduce the outermost experimental moiré structure seen in Fig. 6(b). Building on these findings, a TTG lattice was then considered with θ_3 fixed at 9.8° and θ_2 adjusted to 4.2° , as illustrated in Fig. 13(b) of Appendix C. The simulated real-space and FFT images, produced using the analytical approach, are presented in Figs. 6(b) and 6(d), respectively. These results are in excellent agreement with the experimental images in Figs. 6(a) and 6(c). Specifically, the outermost and innermost moiré patterns are characterized by lattice constants of $A_0 = 14.5 \text{ \AA}$ and $A_1 = 34.0 \text{ \AA}$, closely matching the experimental values of $15.0 \pm 0.5 \text{ \AA}$ and $38.5 \pm 1.5 \text{ \AA}$ extracted from Fig. 5(d). Additionally, the insets in Figs. 6(c) and 6(d) reveal a close alignment of the replicas with the innermost hexagonal spots. Further analysis is limited by the quality of the experimental FFT image in Fig. 6(c).

In summary, the distinctive arrangement of the experimental FFT spots in Figs. 5(c) and 6(c) strongly indicates that NPG regions 2 and 3 are composed of TTG structures. To rule out the involvement of more than three layers, various constant-current STM images and corresponding FFT profiles of twisted four-layer graphene were computed within the framework of the analytical model. An illustrative example is provided in the Supplemental Material [21] (see Fig. S3 and related discussion). In all tested cases, the FFT images of the four-layer structures displays moiré lattices comprising three sets of hexagonal spots and one set of hexagonal replicas, which do not match the observed FFT features.

To further validate this interpretation, the DFT-U approach was employed, using the DFT projected density of graphene and $E_b = -0.8 \text{ eV}$, which matches the experimental bias

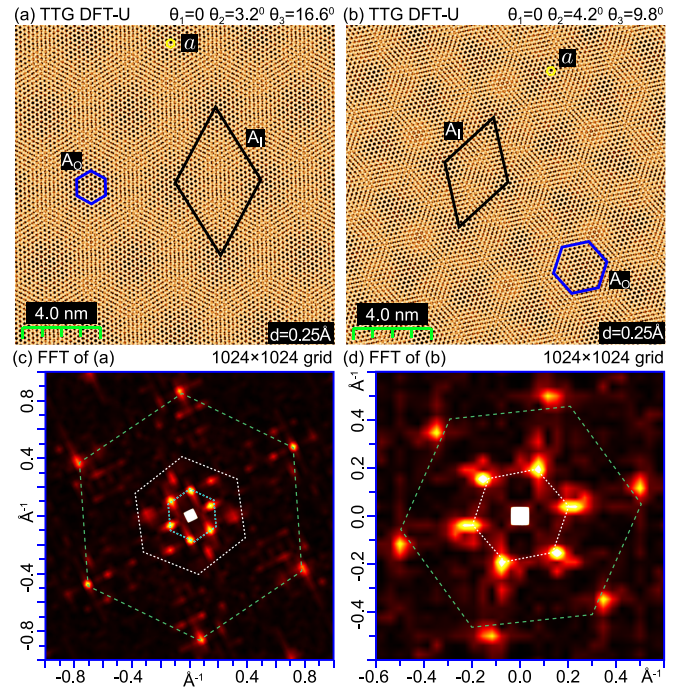


FIG. 7. (a) Constant-current STM image of TTG from DFT-U calculations using Eqs. (4) and (5) with parameters $\theta_1 = 0$, $\theta_2 = 3.2^\circ$, $\theta_3 = 16.6^\circ$, $a = 2.46 \text{ \AA}$, $I_{\text{STM}}/I_0 = 0.030$, and $d = 0.25 \text{ \AA}$. (b) Constant-current STM image computed as in (a), with $\theta_2 = 4.2^\circ$ and $\theta_3 = 9.8^\circ$. Darker regions in both (a) and (b) highlight atomic and double moiré periodicities, marked by yellow, black, and cyan contours, corresponding to the patterns in Figs. 5(a), 5(b), 6(a), and 6(b). (c) FFT of (a) on a 1024×1024 grid, zoomed on the moiré region, with extracted lattice constants: $A_0 = 8.60 \text{ \AA}$, $A_R = 24.50 \text{ \AA}$, and $A_1 = 44.0 \text{ \AA}$. (d) FFT of (b) computed as in (c), with extracted lattice constants: $A_0 = 14.5 \text{ \AA}$, $A_R = 36.0 \text{ \AA}$, and $A_1 = 38.0 \text{ \AA}$. Dashed lines in (c) and (d) correspond to experimentally measured regions in Figs. 5(c) and 6(c).

voltage of $V_b = -0.80 \text{ V}$. This time, the projected density of the monolayer was replicated twice to construct a three-layer model, maintaining an interlayer spacing of $d = 0.25 \text{ \AA}$. Following Eq. (4), the projected density of the middle layer was then rotated by θ_2 , and that of the bottom layer by θ_3 . For NPG region 2, DFT-U simulations were performed with $\theta_2 = 3.2^\circ$ and $\theta_3 = 16.6^\circ$, yielding the constant-current STM image in Fig. 7(a) and its corresponding FFT in Fig. 7(c). Similarly, for NPG region 3, DFT-U simulations were conducted with $\theta_2 = 4.2^\circ$ and $\theta_3 = 9.8^\circ$, producing the real-space image and FFT shown in Figs. 7(b) and 7(d). The patterns observed in the darker regions of Figs. 7(a) and 7(b) show excellent agreement with the experimental patterns in Figs. 5(a) and 6(a), respectively. Remarkably, the FFT image in Fig. 7(c) closely matches the experimental FFT in Fig. 5(c), demonstrating a near-perfect agreement in moiré periodicities, specifically in the values of A_0 and A_1 , and a close alignment in the positions of the replicas, thereby surpassing the accuracy of the analytical model. Additionally, the FFT image in Fig. 7(d) aligns well with the experimental FFT in Fig. 6(c), showing nearly identical values of A_0 and A_1 . The findings from both the analytical and DFT-U approaches conclusively

demonstrate that the multilayer images of NPG regions 2 and 3 originate from TTG structures. However, the DFT-U method offers superior reliability compared to the analytical model, as it provides a more accurate representation of the electron density distribution across each layer of the twisted structure. Additionally, the DFT-U approach exhibits greater versatility, as it can be readily extended to model multilayer systems, including materials beyond graphene.

As a final exploration, the role of interlayer correlations in TTG was investigated using DFT, focusing on commensurate configurations with two vertically aligned layers sandwiching a third rotated layer. The analysis in Appendix C shows that, similar to the application of TBG to NPG region 1, the proportionality relation (5) tends to underestimate the tunneling currents from the middle and bottom layers. This observation underscores the need for a parameter-dependent model, such as those developed in this study.

IV. CONCLUSIONS

This study presented a comprehensive examination of NPG samples using constant-current STM to offer detailed atomic-level insights into the material. The challenge arises from the natural rotation and variability in twist angles within the NPG samples. Unlike samples that are precisely controlled and rotated at a large scale [39], NPG samples exhibit locally varying twist angles and curvature, which limits the resolution of STM and FFT images. Nonetheless, the experimental results enabled precise mapping of the graphene layers within NPG, revealing that the samples predominantly consist of TBG domains, with twist angles typically exceeding a few degrees. Additionally, intricate moiré patterns characteristic of TTG domains were observed, whereas single graphene layers were not detected.

An analytical model was employed, utilizing independent electron densities, modelled by a simple analytical formula, from rotated graphene layers, connected by an exponential out-of-plane decay as described in Eqs. (3) and (6). This model demonstrated reasonable agreement with DFT calculations of projected electron densities for TBG and simple TTG configurations, using an exponential decay length of 0.5 Å. Consistent with previous studies [20], this length was optimized to enhance the visibility of atomic and moiré lattice periodicities in the simulated STM images, yielding an unrealistically large value of 5.0 Å. Comparative analysis of real and reciprocal space images with experimental data facilitated the identification of TBG- and TTG-like regions within the NPG samples.

The analytical model was refined by replacing the phenomenological electron density of graphene, as defined by Eqs. (1)–(3), with the projected electron density of the monolayer graphene obtained from DFT calculations, matched to the experimental bias voltage. This DFT-U approach, detailed in Eq. (4), required adjusting the interlayer distance from the expected value of 3.34 Å to an unrealistically small value of 0.25 Å to accurately represent the STM current images and their corresponding FFTs.

Both methods required parameter adjustments to extreme values to account for the limited treatment of coupling in the multilayer system and electron transport. Nevertheless,

because of their efficiency in reproducing experimental features, they offer viable alternatives with decent accuracy to the computationally intensive DFT-based transport calculations [40–45], which remain beyond reach for twisted multilayer graphene structures.

In conclusion, the atomic-scale imaging of NPG provides direct evidence of a scalable material with misaligned, weakly interacting graphene layers, offering potential applications in energy storage and electronics. Furthermore, the integration of experimental insights with the accessible simulation models developed here paves the way for further exploration of twisted layered materials, enhancing our understanding and potential utilization of such systems.

ACKNOWLEDGMENTS

The research was partially supported by: “Progetto STAR 2” (PIR01-00008) of the Italian Ministry of Education, University, and Research (MUR), “Centro Nazionale di Ricerca in High-Performance Computing, Big Data and Quantum Computing”, PNRR 4 2 1.4, CI CN00000013, CUP H23C22000360005, “Ateneo projects of Sapienza University” and JSPS-Kakenhi (Grants No. JP21H02037, No. JP23K17661, and No. JP24H00478), European Union - *Next Generation EU* under the PRIN Grants TUNES (2022NXLTYN) and 2D-FRONTIERS (20228879FT) of MUR. Some authors (A.P., F.M., M.P., and A.S.) wish to acknowledge the ‘Marconi’, ‘Galileo100’ and ‘Leonardo’ high performance computing resources, provided by the CINECA consortium (Italy) [46], within the INF16_npqcd project, under the CINECA-INFN [47] agreement, and the ‘Newton’ high performance computing cluster, provided by the University of Calabria.

APPENDIX A: DFT-BASED AND ANALYTICAL APPROACHES TO STM MODELING OF GRAPHENE

To evaluate the improved accuracy of the DFT-U approach compared to the analytical model, preliminary tests were carried out on graphene, focusing on in-plane (xy) profiles of the STM current at a fixed height (z) above the monolayer. As detailed in Sec. II, DFT calculations were performed on the honeycomb lattice defined by primitive vectors $\mathbf{a}_1 = a(1, \sqrt{3})/2$ and $\mathbf{a}_2 = a(-1, \sqrt{3})/2$, with two inequivalent carbon atoms positioned at the origin and at $-\mathbf{a}_1/3 - \mathbf{a}_2/3$, see Fig. 8. The DFT-calculated electron density was then projected over the one-electron states in the energy interval from $E_b = -0.45$ eV (i.e., with a representative bias voltage of $V_b = -0.45$ V) to the Fermi level and then converted to STM current using Eq. (5). The results were compared with the expression

$$I_{\text{STM}} = I_0 \phi_{\parallel}(x, y) e^{-\frac{|z|}{\lambda}}, \quad (\text{A1})$$

derived from Eqs. (2), (6), and (5). Selected results from this comparison are shown in Fig. 8. In particular, Figs. 8(a)–8(c) demonstrate the sensitivity of the xy profiles of the DFT current to the height of the STM tip. In contrast, the analytical model yields the STM image shown in Fig. 8(d), where the fixed intensity scale applied across all plots effectively suppresses the out-of-plane variation described by Eq. (A1).

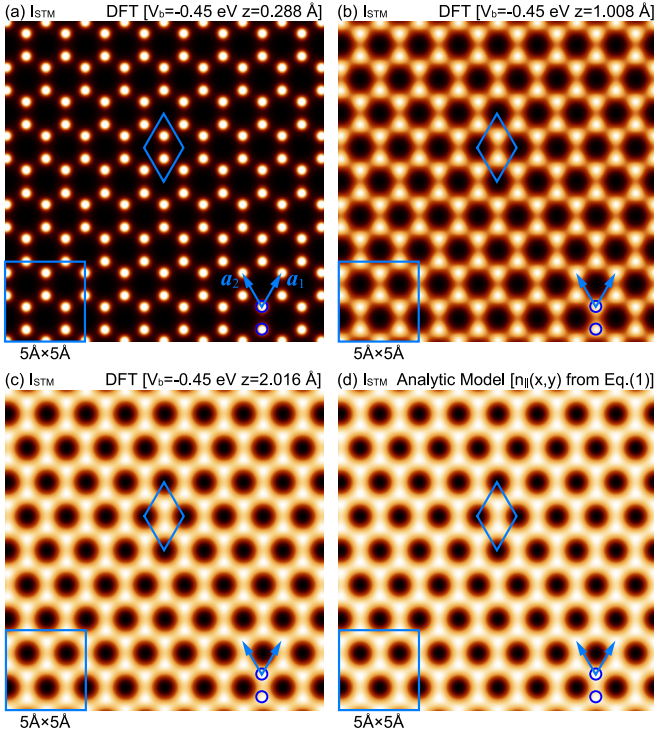


FIG. 8. (a)–(c) DFT simulations of the STM current for graphene at an applied bias voltage of -0.45 V, performed at different constant heights: (a) $z \sim 0.3$ Å, (b) $z \sim 1.0$ Å, and (c) $z \sim 2.0$ Å. (d) Analytic STM current of graphene calculated using Eq. (A1). In all panels, the intensity scale is normalized to unity; arrows denote the primitive vectors \mathbf{a}_1 and \mathbf{a}_2 , and circles indicate the positions of the inequivalent carbon atoms.

Nonetheless, Figs. 8(c) and 8(d) indicate that the DFT calculations exhibit excellent agreement with the analytical model at a height of approximately ~ 2 Å above the graphene plane.

The out-of-plane behavior of the STM current is more accurately captured by examining the z dependence of the biased density, normalized to its maximum. This is illustrated in Fig. 9, which highlights a key result: the analytical approach fails to account for the π symmetry of the Dirac-cone orbitals,

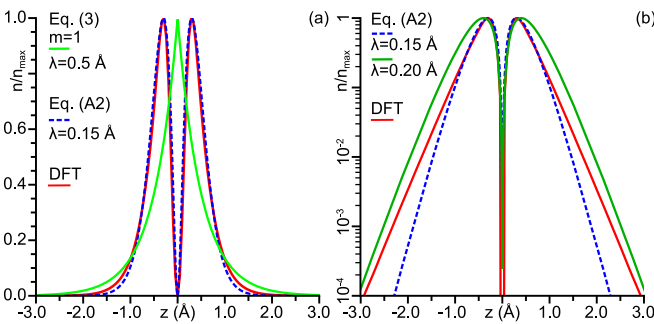


FIG. 9. Out-of-plane (z) variation of the projected electron density of graphene, obtained by: (red) DFT, with $V_b = -0.45$ V; (green) Eq. (3) with $\lambda = 0.5$ Å; (dashed blue) Eq. (A2) with $\lambda = 0.15$ Å and (dark green) Eq. (A2) with $\lambda = 0.20$ Å. The density curves, normalized to their maximum intensities, are plotted on (a) linear and (b) logarithmic scales.

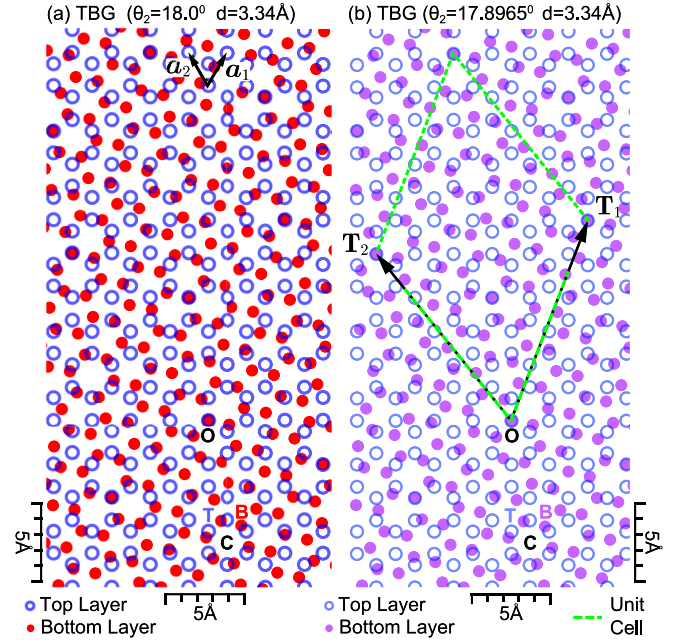


FIG. 10. Top view of TBG lattices with an interlayer distance of $d = 3.34$ Å between the top (unrotated) and bottom (rotated) layers. (a) Incommensurate lattice with a twist angle $\theta_2 = 18.0^\circ$, relative to a rotation axis through aligned hexagonal unit cells at point C. \mathbf{a}_1 and \mathbf{a}_2 label the primitive vectors of the top layer. (b) Commensurate lattice with a twist angle $\theta_2 = 17.8966^\circ$, relative to a rotation axis through aligned sublattice sites at point O. Dashed green lines outline the AA-stacked supercell containing 124 atoms, with primitive vectors \mathbf{T}_1 and \mathbf{T}_2 , each 13.6967 Å in length. Points T (top layer) and B (bottom layer) are nearest neighbors to C. In-plane coordinates of points O, T, and B are referenced in the z -dependent biased density plots in Figs. 4(e)–4(g).

which predominantly determines the graphene electron density at the bias values considered in this paper.

As further illustrated in Fig. 9, the out-of-plane behavior of the DFT-projected density in graphene is more appropriately described by

$$n(x, y, z) = n_0 \phi_{\parallel}(x, y) \frac{z^2}{2\lambda^2} e^{-\frac{|z|}{\lambda}}, \quad (\text{A2})$$

which correctly exhibits a symmetric double-peak structure at $|z| = 2\lambda$ from the graphene plane. This model shows excellent agreement with DFT calculations for λ values ranging from 0.15 Å to 0.20 Å. In contrast, the analytical density described by Eq. (3) with $m = 1$ exhibits a single peak at the graphene plane, requiring large λ values to approximate the out-of-plane trend near $z = 0$.

Thus, the DFT-U model effectively captures the variation in the valence electron density near the graphene plane, whereas the analytical approach, as defined by Eq. (3), requires further refinement to accurately describe this aspect. This distinction highlights why Eq. (4) offers a more precise representation than Eq. (3). However, the analytical model, even in its basic form, provides a straightforward expression for the constant-current STM image via Eq. (6), while the DFT-U method necessitates a more complex numerical inversion to solve Eq. (5).

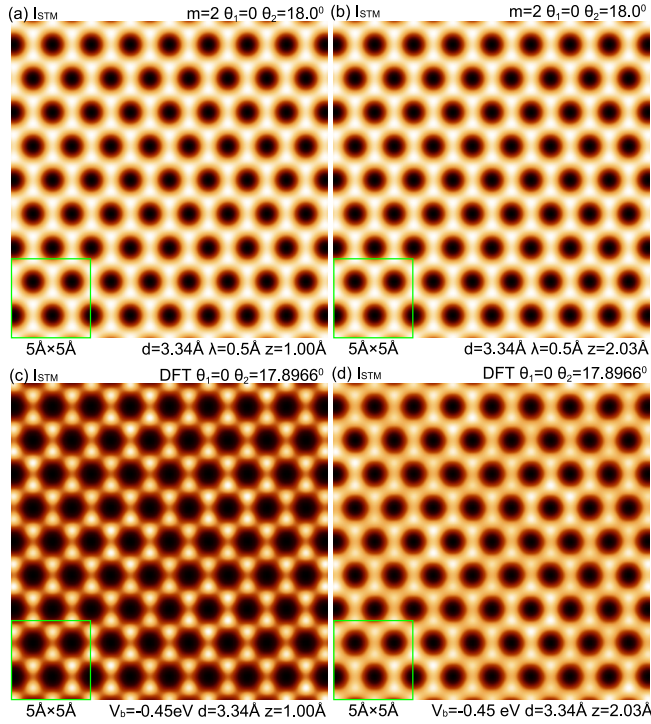


FIG. 11. STM current for TBG at a constant height of (a)(c) $z = 1.00$ Å and (b)(d) $z = 2.03$ Å. The images are obtained using: (a)(b) the analytical approach outlined in Eqs. (3) and (5) with parameters $m = 2$ and $\lambda = 0.5$ Å, applied to the incommensurate lattice of Fig. 10(a); (c)(d) DFT calculations with an applied bias voltage $V_b = -0.45$ V on the commensurate lattice of Fig. 10(b).

APPENDIX B: DFT-BASED AND ANALYTICAL APPROACHES TO STM MODELING OF TBG

Moving from graphene to TBG, various xy profiles of the STM current at a constant height z above the top layer were calculated using Eqs. (3) and (5), with parameters $m = 2$, $\theta_1 = 0$, $\theta_2 = 18.0^\circ$, and $d = 3.34$ Å, which define the quasicrystalline structure shown in Fig. 10(a). Self-consistent DFT calculations were conducted on a commensurate TBG lattice, maintaining the same interlayer distance and a rotational misalignment angle near 18° , within the experimentally observed uncertainty of $\pm 2^\circ$. Among the various commensurate TBG configurations available [23], a moiré supercell was selected, characterized by the primitive vectors $\mathbf{T}_1 = 5\mathbf{a}_1 + \mathbf{a}_2$ and $\mathbf{T}_2 = -\mathbf{a}_1 + 6\mathbf{a}_2$, derived from the lattice basis of the top layer, given in Appendix A. This particular configuration, corresponding to a twist angle of $\theta_2 = 17.8966^\circ$, was chosen because of the relatively small number of atoms in the supercell, specifically 62 atoms per sublattice plane, as indicated in Fig. 10(b).

The STM current predicted by the analytical model exhibits minimal dependence on the tip height, as shown in Figs. 11(a) and 11(b). In contrast, the DFT calculations demonstrate a pronounced sensitivity to z . At $z = 1.0$ Å, the STM current sharply peaks at the lattice positions of the top layer, as illustrated in Fig. 11(c), but this sharpness diminishes significantly, resulting in a smeared distribution around these positions at $z = 2.03$ Å, as shown in Fig. 11(d). Notably, Figs. 11(b) and 11(d) indicate that the analytical

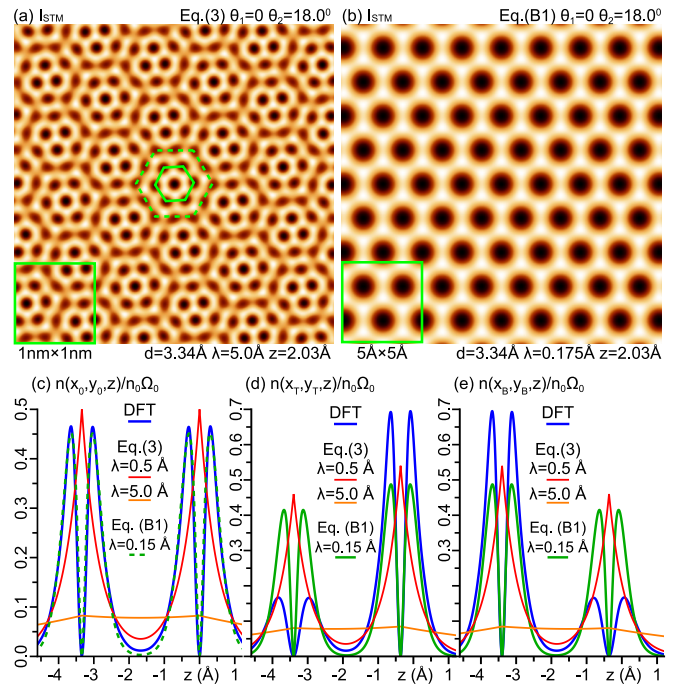


FIG. 12. (a) STM current for TBG in the incommensurate lattice of Fig. 10(a), calculated using Eq. (3) with a twist angle $\theta_2 = 18^\circ$, at a height $z = 2.03$ Å, and an attenuation length $\lambda = 5.0$ Å. (b) STM current calculated using Eq. (B1), under the same conditions as (a) but with $\lambda = 0.175$ Å. (c)–(e) Out-of-plane (z) profiles of the projected electron density obtained via DFT, Eq. (3) with $\lambda = 0.5$ Å and $\lambda = 5.0$ Å, and Eq. (B1) with $\lambda = 0.15$ Å. All density curves are normalized to the same unit area, with the z axis passing through the in-plane coordinates of the points O, τ , and B, as shown in Fig. 10. The same coordinates are used in the projected density plots of Figs. 4(e)–4(g).

model reasonably aligns with the DFT results at $z \sim 2.0$ Å. Furthermore, a comparison between Figs. 8 and 11 reveals that the STM images are predominantly influenced by the top layer, with the contribution of the bottom (twisted) layer largely obscured.

In Sec. III, an increased attenuation length of $\lambda = 5.0$ Å was employed to improve the visibility of FFT spots within the moiré pattern. The resulting STM constant-current image is discussed in Fig. 3(a) of the main text, while the corresponding constant- z STM image is presented in Fig. 12(a). As pointed out in Appendix A, a more accurate model for the projected electron density $n(x, y, z)$, given by Eq. (3), should incorporate a $|z - z_i|^2$ factor to weight the exponential term, reflecting the π -orbital symmetry of the occupied Dirac cone states. This refinement leads to the corrected expression

$$n(x, y, z) = \frac{n_0}{m} \sum_{i=1}^m \phi_{\parallel}(x_i, y_i) \frac{|z - z_i|^2}{2\lambda^2} e^{-|z - z_i|/\lambda}, \quad (\text{B1})$$

which reduces to Eq. (A2) for $m = 1$. As also observed in Appendix A and further illustrated in Figs. 12(b)–12(e), the optimal value of λ using this refined approach lies between 0.15 Å and 0.20 Å.

Notably, the STM current shown in Fig. 12(b), calculated using Eq. (B1) with $\lambda = 0.175$ Å at $z = 2.03$ Å, exhibits a

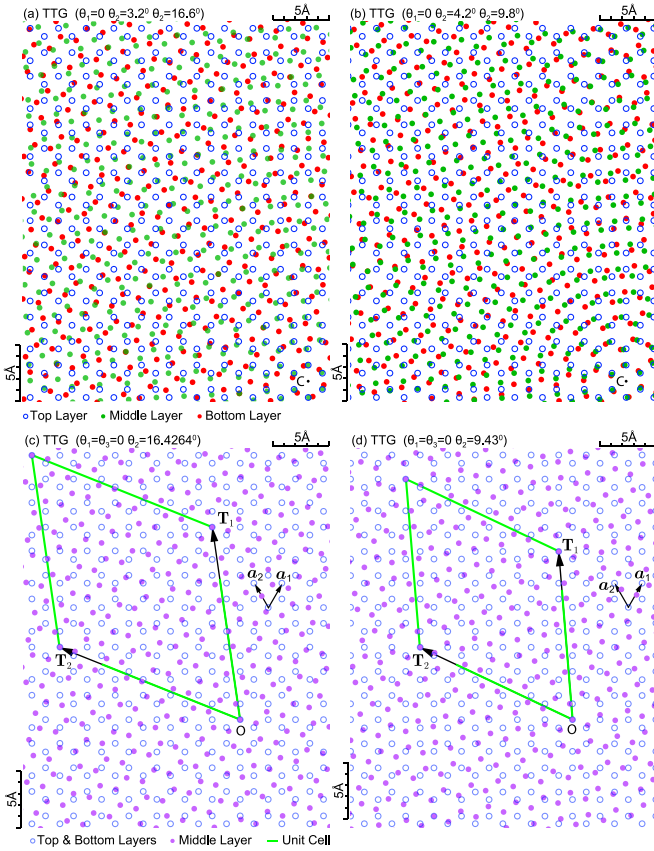


FIG. 13. Top view of TTG lattices with an interlayer distance of $d = 3.34$ Å. Incommensurate configurations with $\theta_1 = 0$, featuring twist angles of (a) $\theta_2 = 3.2^\circ$, $\theta_3 = 16.6^\circ$, and (b) $\theta_2 = 4.2^\circ$, $\theta_3 = 9.8^\circ$. The rotation axis in these cases passes through aligned hexagonal unit cells at point C. Commensurate configurations with $\theta_1 = \theta_3 = 0$ and twist angles of (c) $\theta_2 = 16.4264^\circ$ and (d) $\theta_2 = 9.43^\circ$. Here, the rotation axis passes through aligned sublattice sites at point O. In (c) and (d), \mathbf{a}_1 and \mathbf{a}_2 denote the primitive vectors of the top and bottom layers. Green lines outline the moiré unit cells, containing (c) 98 and (d) 74 atoms per graphene sheet. Primitive vectors \mathbf{T}_1 and \mathbf{T}_2 define these supercells, with (c) $T_1 = T_2 = 17.22$ Å and (d) $T_1 = T_2 = 14.9636$ Å.

close agreement with the corresponding DFT result presented in Fig. 11(d). Moreover, the out-of-plane variation in the DFT projected density is more accurately captured by Eq. (B1) with $\lambda = 0.15$ Å compared to Eq. (3) with $\lambda = 0.5$ Å, as seen in Figs. 12(c)–12(e), using the same in-plane coordinates as Figs. 4(e)–4(g). However, while increasing λ to 5.0 Å in Eq. (3) enhances the visibility of the lower graphene layer, applying a similar increase in Eq. (B1) results in the displacement of the double-peaked structures, centered at the TBG layers, to unphysically large z values. A possible workaround is to adjust the interlayer distance as an additional fitting parameter.

In summary, Eq. (B1) provides a more accurate representation of the DFT-calculated electron density, whereas the analytical model defined by Eqs. (3)–(6) allows for the tuning of a single parameter, λ , to enhance the visibility of FFT spots originating from misaligned layers.

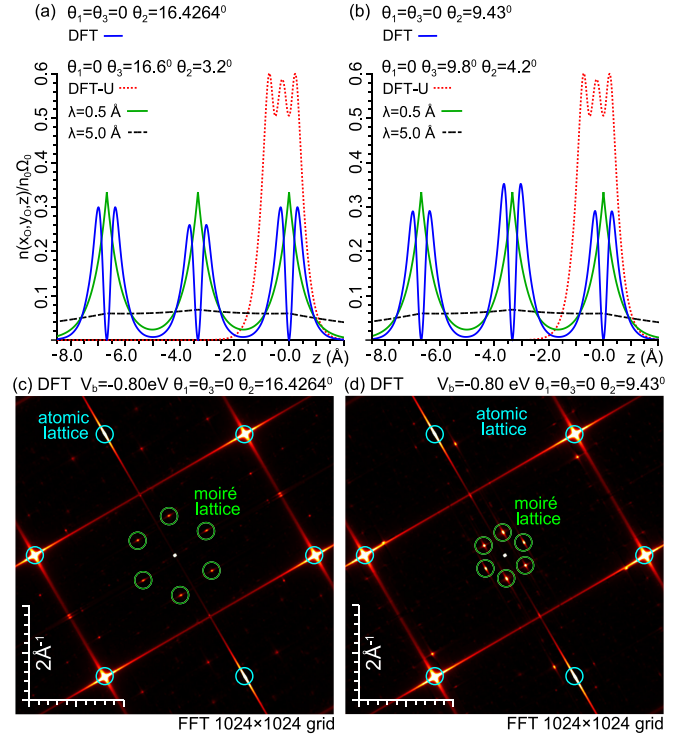


FIG. 14. [(a),(b)] Projected density of TTG, computed using DFT, DFT-U, and analytical methods along the axis passing through the top, middle, and bottom lattice sites. [(c),(d)] FFTs of constant-current STM images, computed using DFT as described in Sec. II. DFT calculations were performed on the commensurate lattices shown in Figs. 13(c) for (a) and (c), and Fig. 13(d) for (b) and (d). DFT-U calculations in (a) and (b) used the same parameters as Figs. 7(a) and 7(b), respectively. The analytical model in (a) and (b) was applied using the same parameters as Figs. 5(b) and 6(b), including $\lambda = 0.5$ Å.

APPENDIX C: DFT-BASED APPROACHES TO STM MODELING OF TTG

DFT computations on TTG were restricted to simple commensurate configurations, where the top and bottom layers are aligned ($\theta_1 = \theta_3 = 0$), with only the middle layer rotated by θ_2 . Two specific commensurate TTG structures were analyzed, featuring twist angles of $\theta_2 = 16.4264^\circ$ and $\theta_2 = 9.43^\circ$. These angles closely correspond to the largest twist angles observed in the incommensurate TTG lattices depicted in Figs. 13(a) and 13(b), which were used in Sec. III to interpret the STM measurements in Figs. 5(a) and 6(a) using both DFT-U and analytical approaches. For the commensurate lattice with $\theta_2 = 16.4264^\circ$, the primitive vectors are $\mathbf{T}_1 = 3\mathbf{a}_1 + 5\mathbf{a}_2$ and $\mathbf{T}_2 = 8\mathbf{a}_2 - 5\mathbf{a}_1$, resulting in a unit cell containing 294 atoms, as illustrated in Fig. 13(c). Similarly, for the commensurate lattice with $\theta_2 = 9.43^\circ$, the primitive vectors are $\mathbf{T}_1 = 3\mathbf{a}_1 + 4\mathbf{a}_2$ and $\mathbf{T}_2 = 7\mathbf{a}_2 - 4\mathbf{a}_1$, forming a unit cell with 222 atoms, as shown in Fig. 13(d). In both cases, the rotation axis passes through aligned sublattice sites in the top, middle, and bottom layers. The computational effort required to obtain the DFT projected densities for these commensurate TTG structures was comparable to that of the TBG calculations described in Appendix B.

The projected density profiles for these configurations, computed with a bias voltage of $V_b = -0.80$ eV, are presented in Fig. 14(a) for the lattice in Fig. 13(a), and in Fig. 14(b) for the lattice in Fig. 13(b). These results are compared with projected densities obtained from the analytical and DFT-U models, corresponding to NPG region 2 in Fig. 14(a), and NPG region 3 in Fig. 14(b), as discussed in Sec. III. As previously noted in the discussion of Figs. 4(e)–4(g), full DFT calculations provide a highly accurate description of the electron density across and between the TTG layers. The analytical model, using $\lambda = 0.5$ Å, offers a reasonable approximation but fails to capture the π -orbital character typical of the valence electrons in graphene within the TTG layers. In contrast, with $\lambda = 5.0$ Å, the analytical model produces a nearly flat distribution, increasing the contribution to the simulated current from the middle and bottom layers and artificially compensating for the missing transport component in the tunneling current. The DFT-U biased density, compressed

to approximately ~ 3 Å owing to the reduced interlayer separation of $d = 0.25$ Å, accurately estimates the STM current contribution from the middle and bottom layers. Moreover, constant-current STM images, obtained using the method described in Sec. III, but not shown here, are visually indistinguishable from those in Fig. 4(a), reinforcing the conclusion that the top layer dominates, with no visible moiré superlattice. The FFTs of constant-current STM images, shown in Figs. 14(c) and 14(d), exhibit excellent agreement with the outer moiré periodicities observed in Figs. 6(c) and 6(d), while the absence of inner periodicities reflects the single twist angle considered, with $\theta_3 = 0$. In summary, the DFT-U approach effectively translates the overestimation of λ into an underestimation of d , resulting in notable differences in STM current profiles between the analytical and DFT-U methods in the z direction, as illustrated in Figs. 4(e)–4(g), 14(a), and 14(b). Nonetheless, both methods predict STM images and their corresponding FFTs with varying levels of accuracy.

-
- [1] L. Jiang and Z. Fan, Design of advanced porous graphene materials: From graphene nanomesh to 3D architectures, *Nanoscale* **6**, 1922 (2014).
- [2] S. Gadipelli and Z. X. Guo, Graphene-based materials: Synthesis and gas sorption, storage, and separation, *Prog. Mater. Sci.* **69**, 1 (2015).
- [3] Y. Zhu, S. Murali, M. D. Stoller, K. Ganesh, W. Cai, P. J. Ferreira, A. Pirkle, R. M. Wallace, K. A. Cychoz, M. Thommes *et al.*, Carbon-based supercapacitors produced by activation of graphene, *Science* **332**, 1537 (2011).
- [4] A. K. Geim and K. S. Novoselov, The rise of graphene, *Nat. Mater.* **6**, 183 (2007).
- [5] T. H. Han, Y. K. Huang, A. T. L. Tan, V. P. David, and J. Huang, Steam etched porous graphene oxide network for chemical sensing, *J. Am. Chem. Soc.* **133**, 15264 (2011).
- [6] N. S. Safron, M. Kim, P. Gopalan, and M. S. Arnold, Barrier-guided growth of micro- and nano-structured graphene, *Adv. Mater.* **24**, 1041 (2012).
- [7] M. D. Fischbein and M. Drndic, Electron beam nanosculpting of suspended graphene sheets, *Appl. Phys. Lett.* **93**, 113107 (2008).
- [8] Y. Ito, Y. Tanabe, H.-J. Qiu, K. Sugawara, S. Heguri, N. H. Tu, K. K. Huynh, T. Fujita, T. Takahashi, K. Tanigaki, and M. Chen, High-quality three-dimensional nanoporous graphene, *Angew. Chem. Int. Ed.* **53**, 4822 (2014).
- [9] D. Suzuki, T. Okamoto, J. Li, Y. Ito, T. Fujita, and Y. Kawano, Terahertz and infrared response assisted by heat localization in nanoporous graphene, *Carbon* **173**, 403 (2021).
- [10] I. Di Bernardo, G. Avvisati, C. Chen, J. Avila, M. C. Asensio, K. Hu, Y. Ito, P. Hines, J. Lipton-Duffin, L. Rintoul *et al.*, Two-dimensional hallmark of highly interconnected three-dimensional nanoporous graphene, *ACS Omega* **2**, 3691 (2017).
- [11] I. Di Bernardo, G. Avvisati, C. Chen, J. Avila, M. C. Asensio, K. Hu, Y. Ito, P. Hines, J. Lipton-Duffin, L. Rintoul *et al.*, Topology and doping effects in three-dimensional nanoporous graphene, *Carbon* **131**, 258 (2018).
- [12] M. M. S. Abdelnabi, C. Izzo, E. Blundo, M. G. Betti, M. Sbroscia, G. Di Bella, G. Cavoto, A. Polimeni, I. García-Cortés, I. Rucandio *et al.*, Deuterium adsorption on free-standing graphene, *Nanomaterials* **11**, 130 (2021).
- [13] M. G. Betti, E. Placidi, C. Izzo, E. Blundo, A. Polimeni, M. Sbroscia, J. Avila, P. Dudin, K. Hu, Y. Ito *et al.*, Gap opening in double-sided highly hydrogenated free-standing graphene, *Nano Lett.* **22**, 2971 (2022).
- [14] H. Kim, Y. Choi, C. Lewandowski, A. Thomson, Y. Zhang, R. Polski, K. Watanabe, T. Taniguchi, J. Alicea, and S. Nadj-Perge, Evidence for unconventional superconductivity in twisted trilayer graphene, *Nature (London)* **606**, 494 (2022).
- [15] C. Zhang, T. Zhu, S. Kahn, S. Li, B. Yang, C. Herbig, X. Wu, H. Li, K. Watanabe, T. Taniguchi *et al.*, Visualizing delocalized correlated electronic states in twisted double bilayer graphene, *Nat. Commun.* **12**, 2516 (2021).
- [16] Y. Cao, V. Fatemi, S. Fang, K. Watanabe, T. Taniguchi, E. Kaxiras, and P. Jarillo-Herrero, Unconventional superconductivity in magic-angle graphene superlattices, *Nature (London)* **556**, 43 (2018).
- [17] J. Tersoff and D. R. Hamann, Theory of the scanning tunneling microscope, *Phys. Rev. B* **31**, 805 (1985).
- [18] J. Bardeen, Tunneling from a many-particle point of view, *Phys. Rev. Lett.* **6**, 57 (1961).
- [19] R. Hentschke, B. L. Schürmann, and J. P. Rabe, Molecular dynamics simulations of ordered alkane chains physisorbed on graphite, *J. Chem. Phys.* **96**, 6213 (1992).
- [20] F. Joucken, F. Frising, and R. Sporcken, Fourier transform analysis of STM images of multilayer graphene Moiré patterns, *Carbon* **83**, 48 (2015).
- [21] See Supplemental Material at <http://link.aps.org/supplemental/10.1103/PhysRevB.111.045432> for FFT analysis of TBG using the analytical approach with varying attenuation lengths; STM characterization of TBG domains in NPG; constant-current STM images from twisted four-layer graphene in the analytical approach; Supplemental Figs. S1–S3; and Supplemental Table S1.

- [22] I. Horcas, R. Fernández, J. M. Gómez-Rodríguez, J. Colchero, J. Gómez-Herrero, and A. M. Baro, WSXM: A software for scanning probe microscopy and a tool for nanotechnology, *Rev. Sci. Instrum.* **78**, 013705 (2007).
- [23] J. M. B. Lopes dos Santos, N. M. R. Peres, and A. H. Castro Neto, Continuum model of the twisted graphene bilayer, *Phys. Rev. B* **86**, 155449 (2012).
- [24] T. Ohta, J. T. Robinson, P. J. Feibelman, A. Bostwick, E. Rotenberg, and T. E. Beechem, Evidence for interlayer coupling and Moiré periodic potentials in twisted bilayer graphene, *Phys. Rev. Lett.* **109**, 186807 (2012).
- [25] C. Liu, Z. Li, R. Qiao, Q. Wang, Z. Zhang, F. Liu, Z. Zhou, N. Shang, H. Fang, M. Wang *et al.*, Designed growth of large bilayer graphene with arbitrary twist angles, *Nat. Mater.* **21**, 1263 (2022).
- [26] P. Giannozzi, S. Baroni, N. Bonini, M. Calandra, R. Car, C. Cavazzoni, D. Ceresoli, G. L. Chiarotti, M. Cococcioni, I. Dabo *et al.* QUANTUM ESPRESSO: A modular and open-source software project for quantum simulations of materials, *J. Phys.: Condens. Matter* **21**, 395502 (2009).
- [27] P. Giannozzi, O. Andreussi, T. Brumme, O. Bunau, M. B. Nardelli, M. Calandra, R. Car, C. Cavazzoni, D. Ceresoli, M. Cococcioni *et al.*, Advanced capabilities for materials modelling with QUANTUM ESPRESSO, *J. Phys.: Condens. Matter* **29**, 465901 (2017).
- [28] J. P. Perdew, K. Burke, and M. Ernzerhof, Generalized gradient approximation made simple, *Phys. Rev. Lett.* **77**, 3865 (1996).
- [29] D. R. Hamann, Optimized norm-conserving Vanderbilt pseudopotentials, *Phys. Rev. B* **88**, 085117 (2013).
- [30] D. Marchiani, R. Frisenda, C. Mariani, M. Sbroscia, T. Caruso, O. De Luca, M. Papagno, D. Pacilé, S. Jeong, Y. Ito, and M. G. Betti, Charge effects and electron-phonon coupling in potassium-doped graphene, *ACS Omega* **9**, 39546 (2024).
- [31] L. Malard, M. Pimenta, G. Dresselhaus, and M. Dresselhaus, Raman spectroscopy in graphene, *Phys. Rep.* **473**, 51 (2009).
- [32] A. C. Ferrari, J. C. Meyer, V. Scardaci, C. Casiraghi, M. Lazzeri, F. Mauri, S. Piscanec, D. Jiang, K. S. Novoselov, S. Roth, and A. K. Geim, Raman spectrum of graphene and graphene layers, *Phys. Rev. Lett.* **97**, 187401 (2006).
- [33] L. Graziotto, F. Macheda, T. Venanzi, G. Marchese, S. Sotgiu, T. Ouaj, E. Stellino, C. Fasolato, P. Postorino, M. Metzelaars *et al.*, Infrared resonance Raman of bilayer graphene: Signatures of massive fermions and band structure on the 2D peak, *Nano Lett.* **24**, 1867 (2024).
- [34] D. Tománek, S. G. Louie, H. J. Mamin, D. W. Abraham, R. E. Thomson, E. Ganz, and J. Clarke, Theory and observation of highly asymmetric atomic structure in scanning-tunneling-microscopy images of graphite, *Phys. Rev. B* **35**, 7790 (1987).
- [35] J. M. Campanera, G. Savini, I. Suarez-Martinez, and M. I. Heggge, Density functional calculations on the intricacies of Moiré patterns on graphite, *Phys. Rev. B* **75**, 235449 (2007).
- [36] J. M. B. Lopes dos Santos, N. M. R. Peres, and A. H. Castro Neto, Graphene bilayer with a twist: Electronic structure, *Phys. Rev. Lett.* **99**, 256802 (2007).
- [37] E. J. Mele, Commensuration and interlayer coherence in twisted bilayer graphene, *Phys. Rev. B* **81**, 161405(R) (2010).
- [38] S. Shallcross, S. Sharma, E. Kandelaki, and O. A. Pankratov, Electronic structure of turbostratic graphene, *Phys. Rev. B* **81**, 165105 (2010).
- [39] T. Benschop, T. A. de Jong, P. Stepanov, X. Lu, V. Stalman, S. J. van der Molen, D. K. Efetov, M. P. Allan, Measuring local moiré lattice heterogeneity of twisted bilayer graphene, *Phys. Rev. Res.* **3**, 013153 (2021).
- [40] O. Paz and J. M. Soler, Efficient and reliable method for the simulation of scanning tunneling images and spectra with local basis sets, *Physica Status Solidi B* **243**, 1080 (2006).
- [41] R. Zhang, Z. Hu, B. Li, and J. Yang, Efficient method for fast simulation of scanning tunneling microscopy with a tip effect, *J. Phys. Chem. A* **118**, 8953 (2014).
- [42] A. Gustafsson and M. Paulsson, Scanning tunneling microscopy current from localized basis orbital density functional theory, *Phys. Rev. B* **93**, 115434 (2016).
- [43] G. Doyen, D. Drakova, and M. Scheffler, Green-function theory of scanning tunneling microscopy: Tunnel current and current density for clean metal surfaces, *Phys. Rev. B* **47**, 9778 (1993).
- [44] U. Harbola, J. Maddox, and S. Mukamel, Nonequilibrium superoperator Green's function approach to inelastic resonances in STM currents, *Phys. Rev. B* **73**, 205404 (2006).
- [45] Y. Kwok, G. Chen, and S. Mukamel, STM imaging of electron migration in real space and time: A simulation study, *Nano Lett.* **19**, 7006 (2019).
- [46] <https://www.cineca.it/it>
- [47] <https://www.hpc.cineca.it/news/framework-collaboration-agreement-signed-between-cineca-and-inf/n>